High-Fat Diet and a High Amyloid Load Interact to Induce PKC-α Dependent Synaptic Insulin Resistance

Authors

Alexander Wenger, Tingting Li, Chi Nguyen, Ali Celik, Eleonora Cuboni, Alexander Dityatev, Anna Karpova, Michael R. Kreutz, and Robert Ahrends

Correspondence

robert.ahrends@univie.ac.at

Graphical Abstract

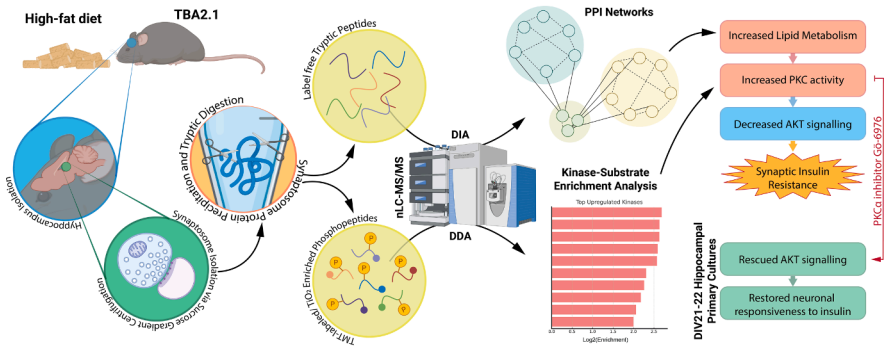

In Brief

Synaptic insulin resistance has been implicated in the progression of Alzheimer's disease, but the underlying molecular mechanisms remain poorly understood. Here, we combined global and phosphoproteomic profiling of hippocampal synaptosomes from wild-type and amyloidogenic transgenic mice exposed to a high-fat diet. Our analysis reveals coordinated remodelling of synaptic lipid metabolism and kinase signalling particularly under combined dietary stress and high amyloid burden. Within this context, protein kinase C-dependent signalling was identified as a key node associated with impaired synaptic insulin signalling.

Highlights

- Deep DIA proteomics quantified over 5400 proteins in hippocampal synaptosomes.
- Combined high-fat diet and amyloid load induce coordinated synaptic lipid metabolic remodelling.
- Phosphoproteomics identifies protein kinase C-dependent signalling linked to insulin desensitization.
- PKCα inhibition restores synaptic insulin responsiveness in neuronal cultures.

2026, Mol Cell Proteomics *25(4)*, 101537

https://doi.org/10.1016/j.mcpro.2026.101537

High-Fat Diet and a High Amyloid Load Interact to Induce PKC-α Dependent Synaptic Insulin Resistance

Alexander Wenger[1], Tingting Li[1,2], Chi Nguyen[2], Ali Celik[3], Eleonora Cuboni[3], Alexander Dityatev[4], Anna Karpova[3,5], Michael R. Kreutz[3,4,5,6], and Robert Ahrends[1,*]

A plethora of studies suggest that a high-fat diet in combination with a high amyloid load causes synaptic insulin resistance and is a risk factor for Alzheimer's disease. Our understanding of the underlying mechanisms is still fragmented. To gain new insights, we conducted integrated proteomic and phosphoproteomic profiling of hippocampal synaptosomes from WT and a transgenic mouse line with a high amyloid load (heterozygous TBA2.1 mice) that show no overt signs of neurodegeneration and dementia. Mice were fed with a regular or high-fat diet. Data-independent acquisition quantified over 5400 proteins, revealing a stable synaptic proteome across conditions. However, the combination of high amyloid load and high-fat diet triggered coordinated remodeling of lipid metabolism pathways, particularly mitochondrial and peroxisomal fatty acid catabolism. Phosphoproteomic analysis showed pronounced activation of lipid- and stress-responsive kinases, including protein kinase C-α, along with increased inhibitory phosphorylation of insulin receptor substrates (IRS1/2). *In vitro* experiments indicate that blocking protein kinase C-α indeed prevents synaptic insulin resistance in primary neurons. The findings suggest that this proteomic workflow, combined with kinase pathway analysis, can reveal nodal points for interventions in a complex disease state with a trajectory to Alzheimer's disease.

Alzheimer's disease (AD) is a progressive neurodegenerative disease that is the most common cause of dementia worldwide. AD is mainly caused by increased amyloid-ß deposition and Tau phosphorylation with consequent formation of senile plaques and neurofibrillary tangles. Chronic sterile neuroinflammation driven by proinflammatory cytokines like TNF α plays a fundamental role in the progression of the disease (1). The metabolic syndrome (MetS), a metabolic imbalance characterized by both peripheral and central insulin resistance and obesity, has been identified as a risk factor for AD pathology, potentially increasing the prevalence of the disease by up to sevenfold (2).

Synaptic insulin resistance (sIR) in the hippocampus is one of the most relevant hallmarks of cognitive decline in MetS, and a close interaction between sIR, MetS, and AD has been suggested, but the molecular mechanisms of this interplay are currently unknown. AD is at an early stage at the onset of cognitive impairment, occurring before significant neurodegeneration and cell loss, and is characterized by synaptic dysfunction and sterile neuroinflammation (2, 3).

In previous work, we found that degradation of the insulin-receptor substrate (IRS1) underlies synaptic insulin resistance under such conditions (4). The molecular cascade inducing degradation includes reduced neddylation of Cullin-7 and inhibitory phosphorylation of IRS1, but the kinase pathways upstream of these events remained elusive (4). An established *in vivo* mouse model of high-risk aging, characterized by a high amyloid load and chronic sterile neuroinflammation, is represented by heterozygous TBA2.1 mice subjected to a Western diet to induce sIR (4). The TBA2.1 transgenic mouse model over-expresses pGlu-Aβ in neurons and is suitable to model neuronal loss and neurodegeneration, characteristics typical of Alzheimer's disease progression (5). Most importantly, these mice show chronic sterile neuroinflammation at early stages, before the onset of detectable neuronal cell loss (5, 6). Whereas homozygous TBA2.1 mice develop pronounced AD-like neuropathology within a few months (7), heterozygous mice show no overt AD-pathology despite amyloid deposition and inflammation (4, 8). Heterozygous mice fed with a high-fat diet (HFD), however, exhibit early synaptic dysfunction, synaptic IR, and cognitive impairment (4). These findings suggest that dietary modification could play a role in modifying disease trajectories in AD by inducing sIR.

Along with changes in overall protein abundance, both HFD and AD cause shifts in protein phosphorylation, which can

From the [1]Institute of Analytical Chemistry, Department of Chemistry, University of Vienna, Vienna, Austria; [2]Leibniz-Institut für Analytische Wissenschaften – ISAS – e.V., Dortmund, Germany; [3]Research Group Neuroplasticity, Leibniz Institute for Neurobiology, Magdeburg, Germany; [4]German Center for Neurodegenerative Diseases (DZNE), Magdeburg, Germany; [5]Center for Behavioral Brain Sciences, Otto von Guericke University, Magdeburg, Germany; [6]Leibniz Group 'Dendritic Organelles and Synaptic Function', Center for Molecular Neurobiology, ZMNH, University Medical Center Hamburg-Eppendorf, Hamburg, Germany
*For correspondence: Robert Ahrends, robert.ahrends@univie.ac.at.

https://doi.org/10.1016/j.mcpro.2026.101537

commonly be mapped using advanced phosphoproteomic analyses (often using Tandem Mass Tag (TMT)-labeled mass spectrometry) nowadays. For example, a deep phosphoproteome survey across multiple mouse models of amyloidosis found 122 phosphopeptides (on 80 proteins) significantly altered in the cortex at early disease stages, whilst 60% of these phosphoprotein changes occurred without a corresponding change in total protein level. This suggests that AD pathology triggers dysregulation of kinase/phosphatase activities – a "rewiring" of synaptic signaling – rather than simply reflecting protein abundance loss (9).

To decipher these complex interactions and bridge gaps in limited proteomic data on newer AD models like TBA2.1, we utilized data independent acquisition (DIA) proteomics and TMT-based phosphoproteomics, enabling unbiased and deep coverage of the synaptosome proteome. Unlike previous work, which often analyzes bulk tissue homogenates – thereby mixing signals from neurons, astrocytes, and microglia – we performed synaptosome isolation before analysis. This ensures pinpointing changes in the proteome/phosphoproteome that relate to altered metabolic pathways and observed pathologies at synaptic sites.

In this study, we complement protein abundance data with phosphosite-level signaling changes, enabling the detection of kinase pathway rewiring, particularly in synaptic lipid- and insulin-related signaling pathways. We found that HFD in conjunction with neuroinflammation and a high amyloid load enhances synaptic protein kinase C (PKC)-α mediated phosphorylation events, including inhibitory IRS1 phosphorylation and attenuated AKT-signaling downstream of synaptic insulin receptors. Thus, we identified a nodal point that might serve as a molecular entry point in a complex disease scenario.

EXPERIMENTAL PROCEDURES

Animals

All animal experiments were performed in strict accordance with the European Communities Council Directive 2010/63/EU and were approved by the local regulatory authorities in Saxony-Anhalt, Germany. The TBA2.1 transgenic mice (Trib2<Tg(Thy1-Trh/APP*)2.1Ingm>) were kindly provided by ProBiodrug (5) and were housed in individually ventilated cages (Green line system, Tecniplast), as described previously (4, 6, 8). Age-matched C57BL/6J mice were used as WT controls. Male WT (WT, +/+) and heterozygous (+/Tg) TBA2.1 mice were maintained on standard chow until 8 to 9 weeks of age. Thereafter, animals were assigned to either a regular diet (RD) or a high-fat/high-calorie diet (HFD; Ssniff #E15126–34, Soest, Germany). Mice on the HFD were used for synaptosome preparation once they exhibited a 70% increase in body weight, which was typically achieved after 4 to 5 months of dietary intervention. All mice were between 6 and 8 months old at the time of synaptosome isolation.

Experimental Design and Statistical Rationale

This study investigated the impact of dietary intervention on the proteome of hippocampal synaptosomes and the possible impact of an interaction of synaptic insulin resistance with high amyloid load on synaptic proteostasis. A schematic overview of the workflow is depicted in Figure 1, https://BioRender.com/ub8wu3s; https://BioRender.com/ju5qdiu. The experimental design included four groups: TBA 2.1 mice on a HFD, TBA 2.1 mice on a RD, WT mice on HFD, and WT mice on RD, with three biological replicates per condition to ensure measurement reliability.

For the global DIA proteomics experiment, samples were analyzed in randomized order to minimize potential batch and run-order effects. Indexed retention time (iRT) calibration was performed using the Biognosys iRT retention time standard kit. MS1 survey scans were acquired in addition to DIA MS/MS scans, yielding a total of 2963 MS1 spectra and 80,001 MS2 spectra across the dataset. DIA data were acquired over an m/z range of 300 to 1056 using 27 variable-width isolation windows, with window placement optimized according to precursor density. Overlapping windows were employed to improve precursor selectivity, resulting in a total cycle time of approximately 2.43 s.

To generate the DIA spectral library used for peptide identification and quantification, pooled samples representing all experimental conditions were fractionated and analyzed in 24 separate runs. The resulting spectral library was subsequently used for targeted peptide detection across all DIA measurements.

Data processing followed established proteomics workflows, including pre-filtering to remove low-quality data and imputation to manage missing values. Batch effects in the phospho-proteomic data set were corrected using the RUV-III normalization, whereas the global proteomics data were already normalized during the MS/MS spectra analysis *via* Spectronaut by choosing the 'Cross-Run Normalization' to reduce unwanted technical variation. This approach enabled the detection of significant differences in synaptic protein expression and phosphorylation states associated with diet and genotype, offering insights into diet-dependent mechanisms affecting AD progression at the synaptic level.

Comprehensive Excel tables reporting unprocessed global protein abundances (Supplemental Table S1) and phosphopeptide-level identifications and quantification (Supplemental Table S2) are provided.

Synaptosome Isolation

Synaptosomes were isolated from mouse hippocampal tissue using a differential centrifugation protocol optimized for synaptic enrichment, as described in established methodologies (10, 11). Briefly, mouse brains were rapidly extracted, and the hippocampi were dissected on ice to minimize proteolytic activity and preserve protein integrity. The tissue was homogenized in ice-cold sucrose buffer (0.32 M sucrose, 4 mM hepes, pH 7.4), supplemented with protease and phosphatase inhibitor cocktails to prevent protein degradation and preserve post-translational modifications. The homogenate was initially subjected to low-speed centrifugation at 1000*g* for 10 min at 4 °C to remove nuclei and large cellular debris. The resulting supernatant was then centrifuged at 10,000*g* for 15 min at 4 °C to obtain a crude synaptosomal pellet. This pellet was resuspended in hepes-buffered sucrose solution and layered onto a discontinuous sucrose density gradient composed of 0.85 M, 1.0 M, and 1.2 M. Ultracentrifugation was subsequently performed at 100,000*g* for 2 h at 4 °C. The synaptosome-enriched fraction was collected from the interface between 1.0 M and 1.2 M sucrose layers. The resulting pellet was subsequently washed and resuspended in an appropriate buffer for downstream proteomic analyses.

Protein Extraction and Digestion

Protein extraction from synaptic samples was carried out following the recently established SIMPLEX protocol (12). Briefly, homogenized

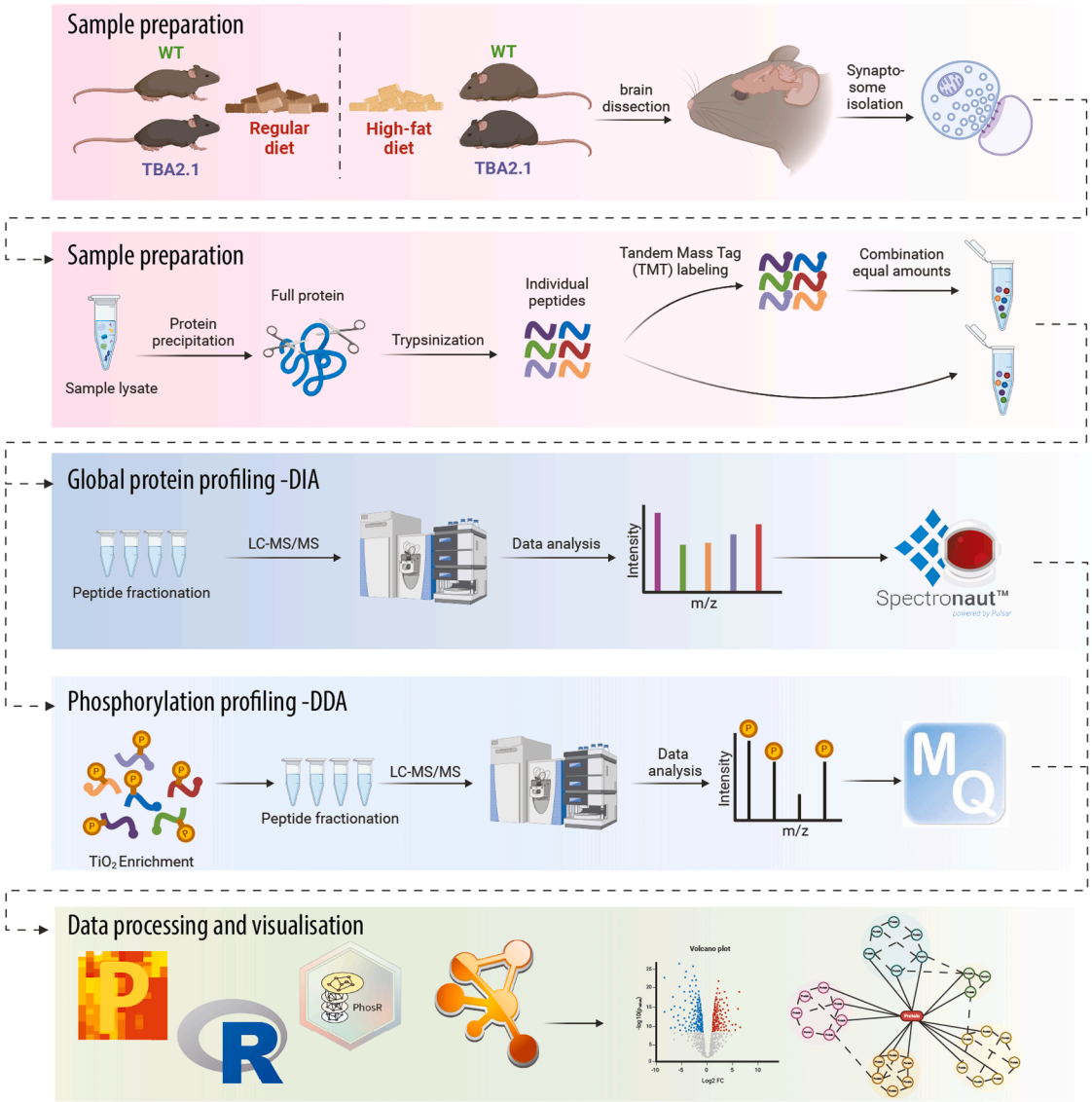

FIG. 1. **Experimental workflow for synaptosome proteome and phosphoproteome profiling in high amyloid load and high-fat diet mouse models.** Schematic overview of sample preparation, mass spectrometry-based analysis, and data processing. *Top panel*: WT and TBA2.1 transgenic Alzheimer's disease model mice were fed either a RD or HFD. Brains were dissected and hippocampal synaptosome fractions were isolated for proteomic analysis. *Middle panel*: Proteins were cleaned-up (filter-aided sample preparation), tryptic digested into peptides, and labeled with Tandem Mass Tags before being forwarded to LC-MS/MS analysis. Global proteomics: For global protein profiling, samples underwent offline fractionation and were analyzed using data independent acquisition (DIA) LC-MS/MS. DIA data were analyzed using Spectronaut software. Phosphoproteomics: For phosphorylation profiling, titanium dioxide -based phosphopeptide enrichment was performed. Samples were also offline fractionated before being analyzed using data-dependent acquisition LC-MS/MS- Phosphosite quantification was performed using MaxQuant. *Bottom panel*: Downstream data processing included normalization, imputation, batch correction, and statistical testing using R, PhosR, and related packages. Visualizations included heatmaps, volcano plots, pathway networks, and kinase activity enrichment to elucidate molecular signaling changes under diet and genotype conditions. Figure created in BioRender. Wenger, A. (2025) https://BioRender.com/ub8wu3s. RD, regular diet; HFD, high-fat diet.

synaptosomes were resuspended in 225 µl MeOH(methanol), followed by three freeze-thaw cycles with intermediate ultrasonication. Later, 750 µl MTBE (methyl-tert-butyl-ether) was added to the sample and incubated for 1 h at 950 rpm at 4 °C to extract lipids and metabolites. The upper organic phase was removed after introducing 188 µl dd water and 10,000*g* centrifugation of 10 min at 4 °C. 527 µl MeOH was added to the remaining phase for protein precipitation (2 h, −20 °C). The pellet was collected and resuspended in complete lysis buffer (1% (w/v) SDS, 150 mM NaCl, 50 mM Tris, pH 7.8 and 1× protein inhibition cocktail, 1× Phosphatase inhibitor). BCA protein assay was used for the determination of protein concentration. Next, 150 µg protein of each sample was respectively transferred to fresh Eppendorf tubes for reduction (TCEP, 10 mM final) and alkylation (Iodoacetamide, 30 mM final). Samples were then diluted with 8M Urea-tris (100 mM tris-HCl, pH 8.5) and loaded onto equilibrated 30 kDa Pall spin filters (Centrifugal devices Nanosept). Samples were

washed three times with 50 mM triethylammonium bicarbonate (TEAB) according to filter-aided sample preparation (13). The digestion was conducted at a 1:20 (w/w) trypsin/protein ratio overnight (16h) at 37 °C in 50 mM TEAB, 0.2 M GuHCl, 2 mM CaCl2 buffer (14).

Eventually, tryptic peptides were acidified by adding formic acid and stored at −40 °C until analysis. A monolithic reversed-phase (RP)-18 column was used for evaluation of digestion efficiency and reproducibility in sample generation (15).

TMT Labelling and Phosphopeptide Enrichment

Tryptic peptides were further labeled with the TMTpro 16plex kit (Lot: UJ292953, Thermo Fisher Scientific) to enable multiplexed quantification. Peptides were dried and dissolved in 100 mM TEAB to a final concentration of 1 μg/μl 100 μg of peptides of each sample were used to incubate with 20 μl TMT reagents at room temperature for 1 h 5% hydroxylamine was added to quench the reaction. The same amount of each sample was pooled and desalted using C18 cartridges (Sep-Pak, 50 mg, Waters).

Phosphopeptides were enriched using titanium dioxide following an optimized protocol as previously described (16). Briefly, the pooled peptides were dried and resuspended in a freshly prepared loading buffer (1 M glycolic acid, 80% acetonitrile (ACN), and 5% trifluoracetic acid (TFA)). Enrichment was conducted at a titanium dioxide bead-to-peptide ration of 6:1 by incubating for 10 min at RT. The beads were then collected after centrifugation. This step was repeated twice using half and 1/4 of the amounts of beads previously used. The beads were pooled and then washed with washing buffer (80% ACN, 1% TFA) followed by a second washing step with washing buffer 2 (10% ACN, 1% TFA) to remove non-phosphopeptides. Phosphopeptides were eluted with 1% ammonium hydroxide (pH 11.3). Afterward, the eluates were dried and dissolved using 70% ACN, 2% TFA and then acidified by formic acid (FA) and TFA (pH < 2), followed by desalting using Oligo R3 microcolumns. The desalted phosphopeptides were dried and stored at −40 °C for further analysis.

Phosphopeptide Fractionation

To reduce sample complexity, off-line hydrophilic interaction liquid chromatography was applied to the enriched phosphopeptides as previously described (17). The dried phosphopeptides were reconstituted in 95% ACN, 0.1% TFA and then loaded onto an in-house packed column (TSKamid gel, 250 μm ID, 15 cm length) on an UltiMate 3000 liquid chromatography (LC) system (Thermo Fisher Scientific, Germany). The HPLC was operated at a flow rate of 4 μl/min using a binary gradient (solvent A: 0.1% TFA, 98% ACN, solvent B: 0.1% TFA). The column was equilibrated with 1% solvent B. Phosphopeptides were manually collected at 1 to 2.5 min intervals during the gradient ranging from 15% to 40% of solvent B in 38 min. Phosphopeptides were collected in 15 fractions. All fractions were dried under vacuum and stored at −40 °C until analysis.

Phosphopeptides Analysis, Nano-LC-MS/MS

All hydrophilic interaction liquid chromatography fractions were analyzed by nano-LC-MS/MS in data dependent acquisition mode (DDA) using an Ultimate 3000 RSLC (Thermo Fisher Scientific, Germering, Germany), online coupled to a Q Exactive HF mass spectrometer (Thermo Fisher Scientific). The dried phosphopeptides were resuspended in solvent A (0.1% TFA, 2% CAN) first pre-concentrated on a C18 Acclaim Pepmap trap column (100 μm × 2 cm; Thermo Fisher Scientific), before separated on a C18 Acclaim Pepmap main column (75 μm × 50 cm; Thermo Fisher Scientific) at 250 nl/min and 60 °C using a 120 min linear gradient range from 3 to 35% solvent B (84% ACN, 0.1% FA).

The mass spectrometer was configured in data-dependent acquisition mode. Full scans were acquired at a resolution of 120,000 at m/z 200, covering a mass/charge range of 300 to 1750 m/z, with an automatic gain control (AGC) target of 3.0×10^6 and a maximum injection time (IT) of 120 ms. Precursor ions were isolated using a width of 0.8 m/z and fragmented by higher-energy collision-induced dissociation with a normalized collision energy of 33. The fragment ions were analyzed at a resolution of 60,000 at m/z 200, with an AGC target of 2.0×10^5, an IT of 120 ms, and a Top Speed method width of dynamic exclusion 30 s.

DIA - Spectral Library Creation

The spectral library of DIA was established based prerequisite fractions which were derived from off-line high pH (pH 8.0) reversed-phase fractionation as previously described (11). After digestion, 5 μg tryptic peptides of all conditions (RD, transgenic RD (tgRD), HFD, and transgenic HFD (tgHFD)) were pooled and desalted dried using a vacuum concentrator. The dried peptides were then resuspended in 10 mM ammonium acetate (pH 8.0) and loaded on a C18 RP chromatography column at a flow rate of 12.5 μl/min. The separation and fractionation were performed under a binary gradient system composed of solvent A (10 mM NH_4HCO_3, pH 8.0) and solvent B (84% ACN in 10 mM NH_4HCO_3, pH 8.0) ranging from 3 to 50% of solvent B over 65 min. In total, 24 fractions were collected in combined form in intervals of 60 s. All fractions were dried under vacuum and dissolved in 0.1% TFA, followed by measurements using a nanoLC system (Ultimate 3000 RSLC) coupled to an Orbitrap mass spectrometer (Dionex UltiMate 3000 RSLCnano, Q Exactive HF, Thermo Fisher Scientific).

The peptides were first injected and preconcentrated on a C18 Acclaim Pepmap trap column (100 μm × 2 cm; Thermo Fisher Scientific) for 5 min using 0.1% TFA at a flow rate of 20 μl/min. Separation was carried out on a C18 Acclaim Pepmap main column (75 μm × 50 cm; Thermo Fisher Scientific) at 250 nl/min and 60 °C. A binary linear gradient (solvent A: H_2O with 0.1% FA; solvent B: 84% ACN and 0.1% FA) was applied for peptide separation increasing from 3% to 35% B in 120 min for peptides analysis and from 3% to 42% B in 60 min.

MS survey scans were acquired on the Fusion Lumos using settings as follows: mass spectrometer was operated in DDA with full MS scans from 300 to 1500 m/z at a resolution of 60,000 (Orbitrap). The AGC was set to 3.0×10^6 and the maximum IT to 50 ms. The fragmentation was conducted at a normalized collision energy of 30% (HCD) in each cycle of the acquisition analysis. Fragment ions were acquired at a resolution of 15,000 with an AGC of 5.0×10^4 and a maximum IT of 200 ms.

Global Proteomics – DIA Analysis

The same nano LC-MS/MS setup in the DDA acquisition was used for the DIA approach. Each sample analyzed was mixed with an appropriate amount of iRT standard (Biognosys) peptides and 1 μg of each sample was subjected to the analysis. Full MS scans were acquired at a resolution of 60,000. The AGC was set to 3.0×10^6 and the maximum IT to 20 ms. The MS/MS parameters were set to 20 DIA windows acquired at a resolution 30,000 with an AGC set to 1.0×10^6, a maximum IT of 60 ms and dynamic exclusion 30 s.

MS/MS Data Analysis

The respective MS/MS spectral library from the 24 DIA library runs was created by using default Spectronaut (Biognosis, Software Version 18.3, https://biognosys.com/software/spectronaut/) library generation *via* Pulsar – 'BGS Factory Settings' except for 'Exclude Single Hit Proteins' and 'Calibrate from Empirical RT' activated and

Swiss-Prot *Mus musculus* (201,902) FASTA file (UniProtKB/Swiss-Prot entries only; containing 17,006 protein sequences).

To analyze the global proteomics runs, regular DIA-analysis was chosen in Spectronaut, and the created spectral library (containing 170,601 precursors entries; 110,172 peptide entries and 15,966 decoys) was assigned to all twelve quantification runs using the 'BGS Factory settings' except for excluding single-hit proteins. The data was analyzed using Spectronaut's default dynamic, run-specific precursor and fragment ion mass tolerances automatically determined based on instrument mass accuracy.

TMT labeled phospho-samples identification and quantification was performed by MaxQuant (Version 2.4.13, https://maxquant.org/). The database search was conducted against the mouse UniProt/SwissProt database (version 2021_03, https://www.uniprot.org/ downloaded on 2022–02–03; containing 25,630 protein sequences) using default parameters for the Orbitrap mass spectrometers. After adding the lot-specific 16-plex TMT tag correction factors, the enzyme specificity was set to trypsin/P, allowing for two missed cleavages. Fixed modifications included carbamidomethylation on cysteine (C), while variable modifications included oxidation on methionine (M), acetylation on protein N-termini and phosphorylation of S, T and Y amino acids. The first search peptide mass tolerance was set to 5 ppm, whereas the main search peptide tolerance was lowered to 2.5 ppm. False discovery rate thresholds were set at 0.01 for both peptide and protein levels. Search results were filtered to exclude potential contaminants, reverse hits, and peptides identified solely based on post-translational modifications.

Output files of both datasets (global and phosphoproteomics data) were then filtered for contaminants, log2 transformed and missing values were imputed (according to the Gauss distribution of the data) using Perseus (software version 2.0.11, https://www.biochem.mpg.de/6304220/perseus). Phosphosite abundances were corrected for their respective global protein abundance. Differences between the conditions were elucidated by performing two-sample t-tests.

Primary Hippocampal Cultures

Primary hippocampal neuronal cultures were prepared from mixed-sex *Sprague-Dawley* rat embryos (E18–19; Janvier LABS), following previously described protocols (6). Briefly, neurons were seeded at a density of 30,000 cells per well either onto poly-L-lysine -coated glass coverslips (Sigma-Aldrich) placed in 12-well plastic culture plates (Greiner), or directly onto poly-L-lysine – coated 12-well plastic culture plates at a density of 60,000 cells per well. Cultures were maintained in Dulbecco's Modified Eagle Medium (DMEM; Gibco, Thermo Fisher Scientific) supplemented with 10% fetal calf serum, 1× penicillin-streptomycin, and 2 mM L-glutamine (Gibco). After a 1-h incubation (at 37 °C, 5% CO_2, 95% humidity), the culture medium was replaced with Neurobasal medium supplemented with 1% NeuroCult SM1 (Stemcell Technologies) and 0.5 mM GlutaMAX (Gibco). Cells were maintained under the same incubation conditions until days *in vitro* (DIV) 21 to 22, without the addition of cytosine β-D-arabinofuranoside, a mitotic inhibitor commonly used to suppress glial proliferation. At DIV 21 to 22, cultures were treated for 24 h with a combination of 100 nM insulin (Sigma-Aldrich, #I6634) and 10 ng/ml tumor necrosis factor-alpha (Rat TNFα Recombinant Protein, PeproTech, Thermo Fisher Scientific). Prior to treatment, half of the conditioned Neurobasal medium (NB; Gibco, Gaithersburg, MD) was replaced with fresh, serum-free NB medium. To evaluate insulin responsiveness, cells were preincubated in conditioned NB medium for 1 h, followed by a 15-min treatment with either 100 nM insulin or vehicle control. Where indicated, the PKCα inhibitor Gö-6976 (100 nM; Sigma-Aldrich, #365250) was applied 15 min prior to insulin stimulation. Following pharmacological treatments, neurons cultured on coverslips were fixed and processed for immunohistochemical detection of phosphorylated AKT (pAKT) at synaptic sites. In parallel, cells cultured directly in 12-well plates were washed with phosphate-buffered saline containing phosphatase inhibitors (PhosSTOP, Roche) and lysed in buffer containing 20 mM Tris-HCl (pH 8.0) and 0.1% Triton X-100, supplemented with protease and phosphatase inhibitor cocktails. Cell homogenates from independent wells of the same experimental condition were pooled and subjected to Western blot analysis. Each sample was loaded in duplicate: one membrane was probed for pAKT with anti-phospho-AKT/Ser473 polyclonal rabbit antibodies (Cell Signaling Technology, #9271S; RRID: AB_329826), and the other for total AKT (pan-AKT) anti-(pan)Akt (40D4) monoclonal mouse antibodies (Cell Signaling Technology, #2920; RRID: AB_11476220). Immunodetection signals for both pAKT and pan-AKT were normalized to actin using anti-β-Actin ((AC-15) Sigma, #A-5441. RRID: AB_476744), mouse monoclonal antibodies to control for variations in protein loading, and the pAKT/pan-AKT ratio was subsequently calculated.

Immunocitochemistry and Confocal Imaging

Immunohistochemical detection of synaptic pAKT levels was performed as previously described (4). Briefly, synaptic sites were labelled using polyclonal guinea pig anti-Shank3 antibodies, while dendrites were visualized with mouse monoclonal anti-MAP2 antibodies (clone AP20; Millipore, #MAB3418, RRID: AB_94856). Subsequently, cells were treated with the following secondary antibodies: goat anti-rabbit Alexa Fluor 568 (Thermo Fisher Scientific, #A-11036, RRID: AB_10563566), goat anti-guinea pig Alexa Fluor 647 (Thermo Fisher Scientific, #A-21450, RRID: AB_141882), and goat anti-mouse Alexa Fluor 488 (Thermo Fisher Scientific, #A-11031, RRID: AB_144696). Coverslips were then mounted with Mowiol mounting medium. Image acquisition was performed using a Leica SP8 TCS STED 3× confocal microscope equipped with a pulsed white light laser, as described previously (4, 6, 8, 18). To quantify pAKT levels in dendritic spines, image acquisition was carried out sequentially using excitation wavelengths of 488 nm (MAP2), 568 nm (pAKT), and 633 nm (Shank3). Optical sections were collected along the Z-axis with a step size of 0.20 μm. Fluorescence intensity of pAKT was measured within the Shank3-defined synaptic mask using Fiji software (19), and values were normalized to untreated control conditions to determine relative changes across experimental groups.

RESULTS

Global Proteomic Alterations in Synaptosomes in Response to HFD and High Amyloid Load

To characterize the effects of HFD and high amyloid load on synaptic protein expression, we performed DIA-based global proteomics on isolated synaptosomes from mouse hippocampi across four experimental groups: WT RD, WT HFD, tgRD, and tgHFD (see Fig. 1). Using an optimized DIA workflow, combined with an offline fractionated DIA spectral library and Spectronaut analysis, we identified and quantified 5417 proteins across all samples, covering a broad dynamic range (Supplemental Fig. S1*A*). Prominent synaptic proteins, such as CaMKIIa, Synapsin 1, PSD-95, GluN1, and Shank2 ranked among the proteins with the highest expression levels (Supplemental Fig. S1*A*), confirming the successful enrichment of the synaptosome proteome. Strong pairwise correlations of protein abundances across all conditions (Pearson $r \geq 0.98$; Supplemental Fig. S1, *B–E*) indicated high

reproducibility and supported the conclusion that the synaptic proteome exhibits only subtle remodelling in response to dietary or genetic interventions.

Differentially Expressed Proteins (DEPs) were identified using t-tests with thresholds of $p < 0.05$ and $|\log_2$ fold-change$| > 0.263$ (20%) (Fig. 2, *A–D*). The HFD *versus* RD comparison in WT mice (Fig. 2*A*) revealed 56 DEPs (40 downregulated, 16 upregulated), while the tgRD *versus* RD (Fig. 2*B*) revealed 42 DEPs (31 downregulated, 11 upregulated). The tgHFD *versus* HFD (Fig. 2*C*) contrasts revealed a total of 45 DEPs with more substantial upregulations (35 DEPs) and a shift of proteins, particularly involving lipid

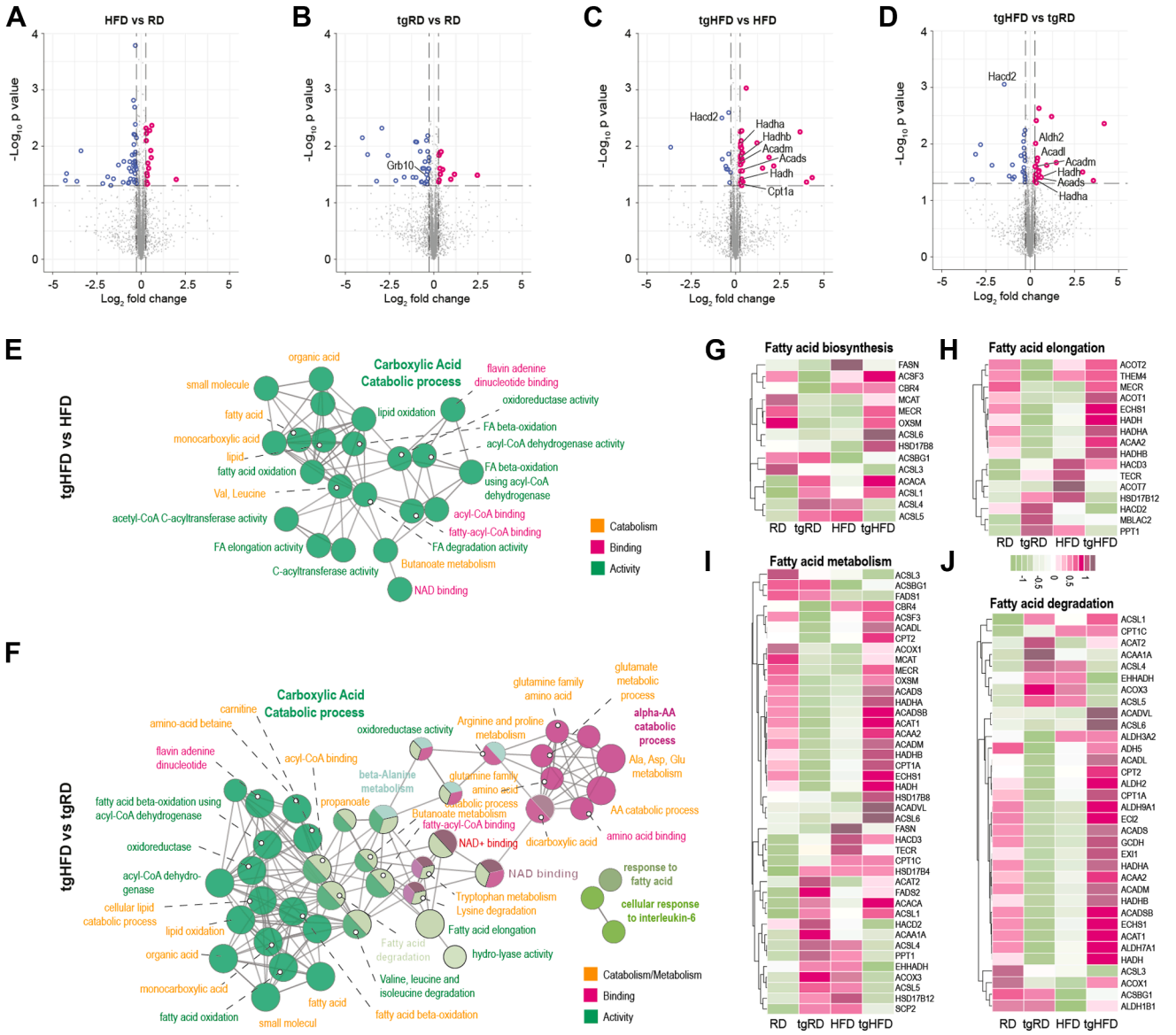

FIG. 2. **Global proteomics analysis of hippocampal synaptosomes reveals diet- and genotype-dependent of synaptic protein content.** *A–D*, volcano plots showing DEPs between experimental groups. Comparisons include: *A,* HFD *versus* RD in WTe mice, *B*, tgRD *versus* RD, *C*, tgHFD *versus* HFD, and *D*, tgHFD *versus* tgRD. Significantly upregulated (*purple*) and downregulated (*blue*) proteins are highlighted ($|\log_2$ fold change$| > 0.264$ (~20%), $p < 0.05$). *E* and *F*, ClueGO enrichment analysis of DEPs for (*E*) tgHFD *versus* HFD and (*F*) tgHFD *versus* tgRD. KEGG pathways (labels altered), Gene Ontology biological processes, and molecular functions are integrated into a unified enrichment network. Node size reflects term significance; functionally related terms are color-coded by ontology group. Enrichment analysis clearly indicates disturbed lipid metabolism, inflammation and oxidative stress. *G–J*, heatmaps showing average normalized protein intensities for lipid metabolism-related pathways derived from KEGG. *G*, fatty acid biosynthesis, (*H*) fatty acid elongation, (*I*) general fatty acid metabolism, and (*J*) fatty acid degradation. Columns represent experimental conditions (RD, HFD, tgRD, tgHFD); rows represent individual pathway genes. Protein expression intensities are color-coded from low (*green*) to high (*purple*). DEP, differentially expressed protein; HFD, high-fat diet; RD, regular diet; tgHFD, transgenic HFD; tgRD, transgenic RD.

metabolism and synaptic signaling components. Additionally, fewer proteins were significantly downregulated (10 DEPs). Comparing tgHFD *versus* tgRD conditions (Fig. 2D) resulted in 57 DEPs (25 downregulated, 32 upregulated), indicating that the presence of the AD genotype is associated with a more coordinated synaptic proteomic response to high-fat diet exposure.

To highlight functional relationships among DEPs, we constructed protein–protein interaction (PPI) networks using the STRING (20) application (version 2.2.0) implemented in Cytoscape (21) (version 3.10.3) using default settings (species: mus musculus, network type: full STRING network, confidence score cutoff: 0.4, maximum additional interactors: 0; singletons not shown). The tgHFD *versus* HFD network (Supplemental Fig. S2*A*) revealed a dense module of enzymes, including Acadvl, Hadha, Hadh, and Cpt1a, implicating enhanced fatty acid metabolism. Similarly, the tgHFD *versus* tgRD network (Supplemental Fig. S2*B*) highlighted proteins involved in both lipid and glucose metabolism, pointing to broader metabolic remodeling in the synapses challenged by amyloid-deposition and HFD. The comparisons for HFD versus RD and tgRD versus RD did not yield any larger functional P-P-I networks (Supplemental Fig. S2, *C* and *D*).

We next performed functional enrichment analysis of comparison-specific DEPs using ClueGO's (22) Cytoscape application (version 2.5.10, https://apps.cytoscape.org/apps/cluego). Hereby, we combined KEGG pathways with biological processes and molecular function ontologies. This approach revealed that DEPs in tgHFD *versus* HFD (Fig. 2*E*) were significantly associated with pathways related to fatty acid β-oxidation, acyl-CoA dehydrogenase activity, and carboxylic acid catabolism. In contrast, tgHFD *versus* tgRD (Fig. 2*F*) showed broader enrichment across lipid and amino acid metabolism, oxidoreductase activity, and immune processes such as response to interleukin-6. These findings indicate that, while the core synaptic proteome remains broadly conserved, the heterozygous TBA2.1 mice kept with a high-fat diet exhibit specific metabolic lipid changes at the synapse.

Since network and pathway analysis of the global proteomic data pointed towards alterations in lipid/fatty acid metabolism and amino acid catabolic processes, we decided to investigate how key enzymes involved in fatty acid metabolism are modulated across conditions. For that purpose, we extracted KEGG pathway gene sets related to fatty acid biosynthesis, elongation, general metabolism, and degradation, and visualized the relative protein abundance using heatmaps of normalized intensities across all four groups (Fig. 2, *G–J*). With this approach, we could show that transgenic mice on HFD (tgHFD) exhibited elevated expressions of several fatty acid converting and degradation enzymes, such as long-chain acyl-CoA synthetases (ACSL5, ACSL6), enzymes responsible for break-down of long-chain fatty acids (HADHB, HADHA) or VLCAD that catalyzes the first oxidative step in the mitochondrial β-oxidation (Fig. 2, *G-J*). However, also enzymes responsible for fatty acid, lipid synthesis are found to be upregulated such as ACAA1, ACAA2, MECR. Based on this observation it can be assumed that we have an increased flux of lipids through the system and likely increased lipid levels in synapses.

Phosphoproteomic Profiling Reveals Kinase Signaling Alterations in Mice with a High Amyloid Load Fed with a High-Fat Diet

To explore kinase signaling pathways responsive to interactions between increased amyloid deposition and HFD, we performed quantitative phosphoproteomics on hippocampal synaptosomes from RD, HFD, tgRD, and tgHFD mouse groups. Filtering the initial dataset (12,620 phosphosites) for only high-confidence sites (localization probability >0.75) and removing potential contaminants resulted in 9277 total phosphosites. Data were imputed following a Gaussian distribution to replace missing values, normalized by global protein abundance, followed by median centering, and batch-corrected using the RUV-III algorithm (23) implemented in the PhosR (24) R package (Supplemental Fig. S1, *F–I*).

Volcano plots of differential phosphosite expression in HFD *versus* RD and tgRD *versus* RD (Fig. 3, *A* and *B*), and in tgHFD *versus* HFD and tgHFD *versus* tgRD comparisons (Fig. 3, *C* and *D*), suggesting that the combination of high amyloid load and HFD distinctively affects phosphorylation of synaptic proteins. Differentially phosphorylated sites were identified using a threshold of $p < 0.05$ and $|\log_2 \text{fold-change}| > 0.264$, corresponding to a ~20% change.

The phosphorylation site sequences, log2 fold-changes, and *p*-values of DEPs were then forwarded to phosphoproteomic enrichment analysis (serine/threonine kinases) using 'The Kinase Library' (https://kinase-library.mit.edu/ea) (25, 26) webpage's 'Phosphoproteomic enrichment analysis' tool. In the tgHFD *versus* HFD comparison (Fig. 3*E*), a striking upregulation of PKC activity, including several isoforms (PKCA, PKCB, PKCE, PKCG, PKCH, PKCI, PKCT, PKCZ) was evident.

Fatty Acid Pathway Rewiring and Insulin Signaling Interference in the Synaptosome of AD Mice under HFD

Since the phosphoproteomic enrichment data showed consistent upregulation of PKC and its isoforms (Fig. 3*E*), we hypothesized that accumulated lipids may activate PKC cascades (27–29) and downstream stress kinases such as Jun N-terminal kinase (JNK) and IKK. PKC activation has been mechanistically linked to the phosphorylation of IRS1 at inhibitory serine residues, disrupting insulin receptor signaling and promoting insulin resistance – a pathway well established in peripheral tissues and emerging in the brain. Especially, PKCα is a key upstream activator of the c-JNK pathway, responsible for phosphorylating IRS1 at inhibitory serine residues (30, 31). This modification disrupts insulin receptor signaling and impairs downstream PI3K–Akt pathway activation, leading to insulin resistance (30). While this mechanism is well-established in peripheral tissues, some evidence

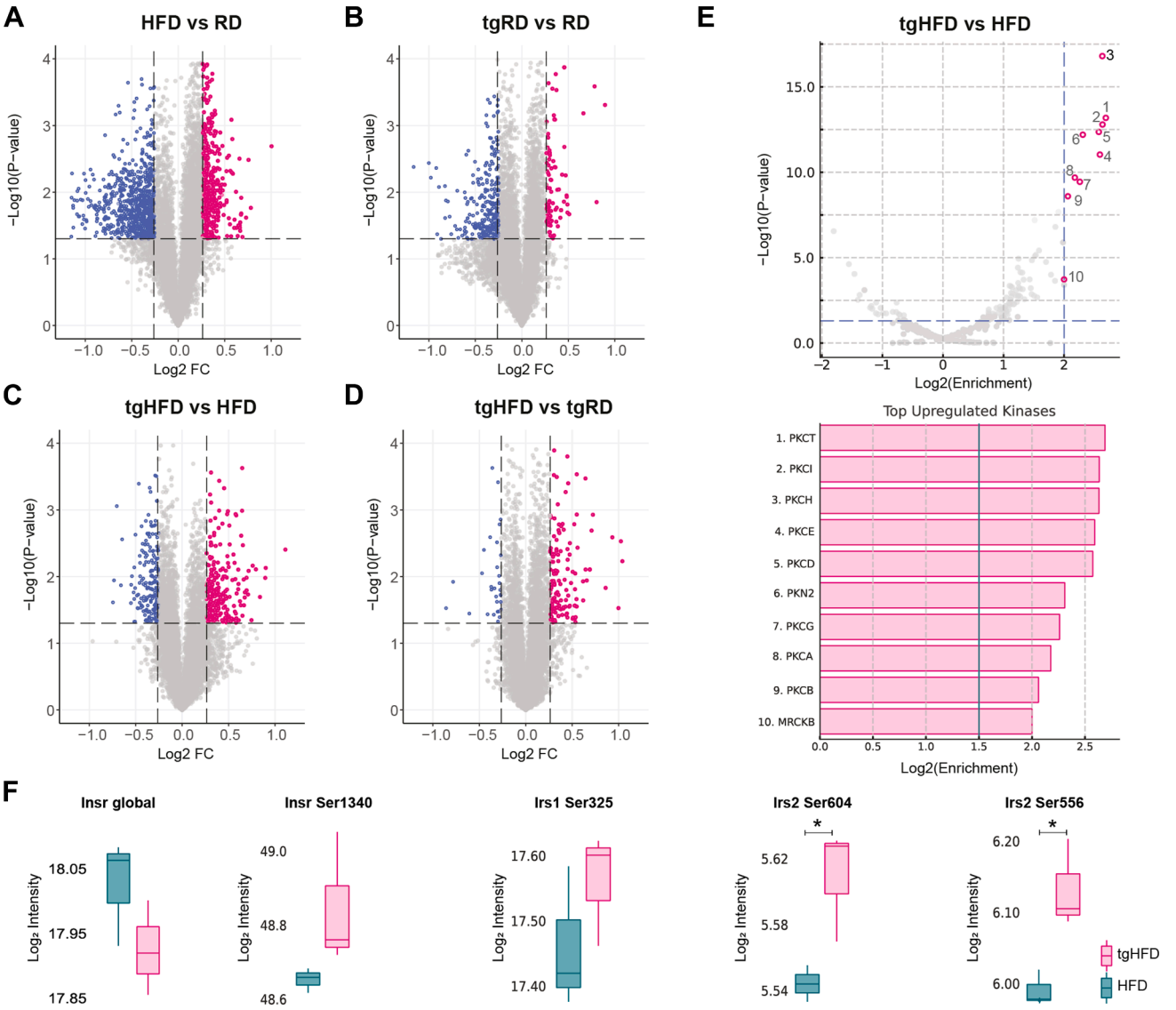

FIG. 3. **Quantitative phosphoproteomics and kinase enrichment analysis reveal altered signaling in AD transgenic synaptosomes under high-fat diet.** *A–D*, volcano plots showing differentially regulated phosphosites across four comparisons: *A*, HFD *versus* RD, (*B*) tgRD *versus* RD, (*C*) tgHFD *versus* HFD, (*D*) tgHFD versus tgRD. Sites with $|\log_2$ fold-change$| > 0.264$ and $p < 0.05$ are colored *pink* (*upregulated*) and turquoise (*downregulated*). *E*, Phosphoproteomic enrichment analysis (KEA3) for tgHFD *versus* HFD reveals top regulated serine/threonine kinases ranked by $\log_2$ enrichment score with a $\log_2$ FC cutoff of '2'. *F*, Boxplots showing normalized $\log_2$ intensities for selected inhibitory phosphosites on Insr (+ global protein level), Irs1 and Irs2 in HFD and tgHFD condition. Sites shown include Insr Ser1340, Irs1 Ser325 and Irs2 Ser604, Ser 556 phosphorylation by PKC (Canonical PKC motifs searched in the phosphoproteomics dataset include RXX[S*/T*], RXRXX[S*/T*] (PKCα/β/γ), and [S*/T*]XR/K (PKCδ/ε/ζ/η/θ). Phosphosite annotations were retrieved from PhosphoSitePlus) and contribute to insulin resistance. Phosphosite-level data were filtered for high-confidence sites (localization probability >0.75), imputed using Gaussian distribution, normalized by median centering, and batch-corrected with RUV-III prior to differential analysis. PKC, protein kinase C; HFD, high-fat diet; RD, regular diet; tgHFD, transgenic HFD; tgRD, transgenic RD.

shows it also occurs in the brain, particularly in AD models (32). To investigate this hypothesis, we mapped our phosphoproteomics dataset to the hypothesized signaling pathway (Supplemental Fig. S2*E*) https://BioRender.com/ub8wu3shttps://BioRender.com/ju5qdiu. Target phosphorylation sites were compared to experimentally validated phosphorylation sites from PhosphoSitePlus (33).

Global proteomic analysis revealed that the steady-state levels of core insulin signaling proteins remained largely unchanged in tgHFD synaptosomes compared to HFD controls (Supplemental Fig. S1*D*) but showed a modest, non-significant reduction in total insulin receptor levels (INSR) (Fig. 3*F*). Phosphoproteomic profiling uncovered distinct post-translational modifications consistent with insulin

resistance. Whereas not statistically significant, we observed a general trend of increased serine phosphorylation of the INSR on its β-subunit at Ser1340 in tgHFD and IRS1 Ser325 (homologous to human Ser330) in IRS1. However, compared to receptor and IRS1; IRS2 protein showed altered phosphorylation at sites known to modulate insulin signaling. Here phosphorylation of Ser556 and Ser604 of IRS2, were significantly elevated in tgHFD synaptosomes (Fig. 3*F*). Phosphorylation of IRS1 Ser330 has been linked to feedback inhibition of insulin signaling, reducing insulin receptor association and downstream PI3K–Akt activation, particularly under insulin-resistant conditions (34). IRS2 Ser556 is a known site that negatively regulates IRS2 activity by limiting its tyrosine phosphorylation (35) and promoting signal termination. IRS2 Ser604 lies within the 14-3-3–binding region and is phosphorylated in response to insulin or IGF-1 stimulation; modification of this residue can alter 14-3-3 recruitment (36), potentially affecting IRS2 stability and availability for receptor docking. Together, elevated phosphorylation at these sites is consistent with feedback attenuation of IRS-dependent insulin signaling under insulin-resistant metabolic stress. Collectively, the pattern of enhanced serine phosphorylation on INSR/IRS suggests a reduced synaptic insulin response in tgHFD.

PKCα (PRKCA), a kinase implicated in insulin desensitization, displayed an approximately 30% decrease in Thr497 phosphorylation (activation loop) in tgHFD synaptosomes when compared to HFD (Supplemental Fig. S2*F*). Changes in activation-loop autophosphorylation site Thr497 therefore reflect altered PKCα activation state, although the static nature of our measurements does not allow discrimination between impaired priming and post-activation dephosphorylation. The loss of PKCα pThr497 suggests chronic PKCα activation in tgHFD (37). In agreement, PKC activation in the liver is a known consequence of lipid oversupply and contributes to insulin resistance by phosphorylating INSR and IRS on inhibitory serines (38).

The PKCα Inhibitor Gö-6976 Prevents Synaptic Insulin Resistance in Vitro

In the final set of experiments, we performed a proof of principle experiment to validate our analysis and to show that our workflow is suitable to generate hypothesis on potential mechanisms upstream of IRS inhibition in synaptic insulin resistance. To this end, we employed an *in vitro* model of synaptic insulin resistance in neuronal primary cultures that we have established previously (4). For this purpose, we included for 24-h insulin and TNF-α in the medium. The rationale of this protocol is that following activation of TNF-α receptor 1, stress kinases such as c-JNK and IκB kinase induce serine phosphorylation of IRS (32), and this has been linked to IR and impaired insulin signaling in neurons (39). In previous work, we found that post-translationally modified pyroglutamylated Aβ3(pE)-42 is taken up by astrocytes, potently induces glial release of TNF-α and thereby causes synaptic dysfunction (8). Hence, the combined administration of insulin and TNF-α resembles the condition of HFD-induced prolonged exposure to insulin and Aβ-mediated neuroinflammation. Synaptic insulin resistance is characterized by reduced phosphorylation of the serine/threonine protein kinase-B/AKT at Ser473 (4). To investigate the role of PKCα in synaptic insulin resistance, we therefore first treated DIV21 to 22 hippocampal primary cultures for 24 h with a combination of 100 nM insulin and 10 ng/ml TNF-α. We then applied the PKCα inhibitor Gö-6976 (100 nM) immediately prior to a 15-min insulin stimulation and assessed cellular responsiveness to insulin by quantifying the pAKT/panAKT ratio (Fig. 4, *A–C*).

As expected, Western blot analysis revealed a marked reduction in the pAKT/pan-AKT ratio in neurons subjected to overnight insulin/TNF-α treatment, suggestive of impaired synaptic insulin signaling and consistent with our previous findings (4). While the *in vitro* experiments model acute insulin desensitization, they engage overlapping signaling nodes with the chronic synaptic insulin resistance observed *ex vivo*, supporting the relevance of these pathways without implying identical physiological states. Intriguingly, inhibition of PKCα with Gö-6976 restored the pAKT/pan-AKT ratio to near-normal levels of neuronal responsiveness to insulin, indicating a prevention of synaptic insulin resistance *in vitro* (Fig. 4, *A–C*). Furthermore, immunocytochemical analysis of pAKT at synaptic sites, identified by anti-Shank3 immunolabeling, revealed restored AKT activation at postsynaptic sites following PKCα inhibition (Fig. 4, *D* and *E*).

DISCUSSION

In this study, we present a proteomic and phosphoproteomic analysis of hippocampal synaptosomes from WT and TBA2.1 mice exposed to either a RD or HFD. Our DIA-based global proteomics workflow achieved deep coverage of the synaptic proteome, consistently quantifying over 5400 proteins. The high reproducibility across replicates indicates that the synaptosome proteome is relatively stable, with only modest remodeling in response to HFD or genotype alone. This is surprising, since early synaptic dysfunction is part of the trajectory towards dementia in AD in high-risk aging characterized by synaptic insulin resistance and high amyloid load. On the other hand, we processed synaptosomes from mice at a very early stage when the impact of sIR is detectable but synaptic dysfunction and cognitive impairment is still rather subtle (4). Thus, we speculate that our data reflects the earliest detectable changes at this stage of disease progression.

The combination of high amyloid load and high-fat diet induces changes in lipid metabolism and kinase pathways

Along these lines, the combination of high-fat diet and the transgenic mouse line appeared to coordinate regulation of

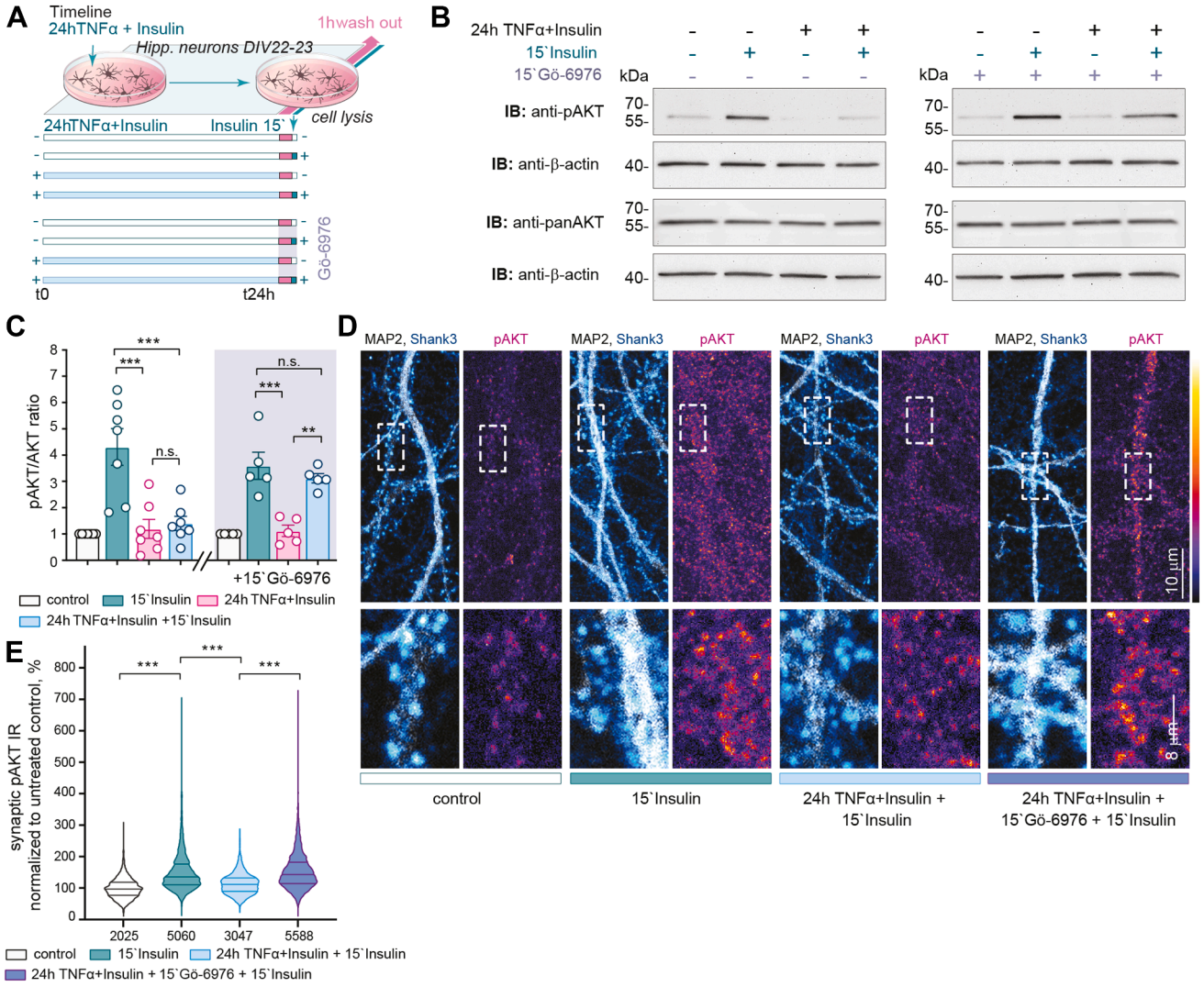

FIG. 4. **Inhibition of PKCα with Gö-6976 preserves neuronal responsiveness to insulin *in vitro*.** *A*, schematic illustrating the experimental timeline and protocol for induction of synaptic insulin resistance. *B*, representative immunoblots probed with antibodies against pAKT (Ser473), pan-AKT, and β-actin the absence (*left panel*) and presence (*right panel*) of the PKCα inhibitor Gö-6976. *C*, quantification of the pAKT (Ser473)/pan-AKT ratio. Statistical analysis was performed using one-way ANOVA followed by a Bonferroni post hoc test. *D*, confocal images showing dendrites of hippocampal neurons immunostained for pAKT (Ser473), MAP2, and Shank3. Synaptic insulin resistance reduced pAKT levels at synapses labeled with Shank3, whereas Gö-6976 treatment restored synaptic pAKT. Pixel intensities (0–255) are presented using a gradient Fire lookup table. The Scale bar represents 10 µm; insets, 8 × 5 µm. *E*, quantification of pAKT intensity at Shank3-positive synaptic sites. Statistical analysis was performed using one-way ANOVA followed by Bonferroni post hoc test.

lipid metabolism pathways, including fatty acid β-oxidation and degradation, especially in the tgHFD group. Network analysis of DEPs revealed a strong enrichment for mitochondrial and peroxisomal lipid catabolism, suggesting that the synapse adapts metabolically to cope with increased lipid burden, as a result of HFD. Whether this is due to greater uptake or a triggered activity needs further investigation. It is known that higher amyloid-beta load leads to an increase in leakage of the blood-brain barrier (40). Consistent with altered lipid handling at synapses, the global proteomics analysis (Fig. 2, *E–J*) revealed that key enzymes involved in mitochondrial and peroxisomal fatty acid β-oxidation and degradation (*e.g.,* ACADL, ACOX1, ECI1) were upregulated in tgHFD mice, indicating an enhanced lipid catabolic response. These findings extend previous reports linking brain lipid metabolism to AD progression and dietary status (41, 42) and increased expression of mitochondrial and peroxisomal fatty-acid β-oxidation enzymes at synapses shown in other AD studies (43). The upregulation of lipid-catabolism pathways suggests that synapses are metabolically adapting to the combined stress of amyloid and excess dietary fat. Such adaptations may temporarily help neurons to cope with a high

lipid load, whereas chronic HFD or alterations in brain lipid metabolism might amplify AD-like pathology and accelerate synapse loss (44, 45).

Whereas the total number of DEPs was generally comparable across the different pairwise comparisons, robust PPI networks emerged primarily in the tgHFD vs. HFD and tgHFD vs. RD contrasts. This reflects the fact that PPI network structure depends not only on the number of DEPs, but critically on their functional relatedness and degree of convergence onto shared molecular pathways or protein complexes. The comparisons largely characterized by isolated nodes (singletons), suggest more heterogeneous or context-specific proteomic changes that do not map onto well-annotated interaction networks. Thus, the presence of connected PPI networks in the tgHFD comparisons likely reflects coordinated perturbations of synaptic protein systems driven by the combined effects of genotype and dietary challenge, rather than differences in statistical power or DEP detection alone.

Moreover, the higher count of singleton nodes in other contrasts may also reflect incomplete coverage of synaptic protein interactions in current PPI databases, particularly for lipid-associated or low-abundance synaptic proteins, further emphasizing that lack of network connectivity does not imply biological irrelevance.

At the post-translational level, phosphoproteomics revealed extensive reprogramming in tgHFD animals compared to controls, with kinase enrichment analysis identifying significant activation of stress-related and lipid-sensitive kinases, notably multiple isoforms of PKC. The enhanced activity across PKC isoforms strongly implicates amyloid pathology and lipid-activated PKC signaling in IRS1/2 inhibition and broader insulin signaling disruption. PKC isoforms are lipid-activated kinases that function in both neurotransmission and metabolic signaling (46, 47).

Although IRS1 was not detected in our global synaptic proteomics dataset, likely reflecting its low abundance in mature mouse hippocampus (48) and limited detectability in untargeted proteomic analyses. Nevertheless, previous studies have reported IRS1 destabilization and degradation in insulin-resistant states and neurodegenerative disease models, suggesting that impaired IRS1 signaling may represent an upstream or parallel mechanism contributing to the synaptic alterations observed here (4, 49). Importantly, the present study focuses on downstream synaptic protein networks rather than direct measurement of IRS1 abundance.

Analysis of the phosphoproteome data provided evidence for site-specific alterations in insulin signaling at hippocampal synapses as a result of the interaction of HFD and amyloid pathology. Increased INSR Ser1340 phosphorylation in combination with a decrease in total INSR protein level suggests altered receptor signaling. The most notable change in IRS1 was the increased phosphorylation at Ser325, a site known to inhibit IRS1-INSR interaction and downstream PI3K/AKT activation (50). We hypothesize that this site is phosphorylated by PKC isoforms under conditions of lipid burden and oxidative stress in hippocampal synapses of tgHFD mice. In addition, IRS2 phosphorylation at Ser556 and Ser604 was increased, while global IRS2 level slightly decreased (Supplemental Fig. S2*F*) in tgHFD mice when compared to controls fed with a high-fat diet without increased amyloid deposition. The site-specific shifts in phosphorylation of IRS1 and 2 suggest a mechanism for sIR, however, the functional consequences require further validation.

Taken together, our data suggest that sIR might be caused by PKC-induced hyperphosphorylation of IRS1/2 and reduced AKT activity.

We next exploited the heuristic value of this data set to test novel hypotheses on underlying mechanisms. To this end, we chose for reasons of feasibility an *in vitro* approach and induced sIR in hippocampal primary neurons. In accordance with previous work, we found that prolonged treatment with insulin and the proinflammatory cytokine TNF-α attenuated insulin-induced AKT activation and resulted in reduced IRS1 protein levels (4). Concomitant application of the PKCα inhibitor Gö-6976 efficiently blocked synaptic insulin resistance as predicted from our kinase network analysis. Thus, our analysis might indeed be useful in identifying molecular entry points for interventions that could be relevant for treating sIR. The proteomic workflow allows testing hypotheses on the underlying mechanisms by which the interaction of high amyloid load, neuroinflammation, and diet-induced obesity causes sIR.

DATA AVAILABILITY

The mass spectrometry proteomics data have been deposited to the ProteomeXchange Consortium *via* the PRIDE partner repository with the dataset identifier PXD069785.

Supplemental data—This article contains supplemental data.

Acknowledgments—We gratefully acknowledge the technical assistance of Corinna Borutzki and Monika Marunde. We also want to thank Tortsen Stöter for developing ImageJ macros for the ICC analysis of pAKT at synapses.

Funding and additional information—Work in the lab of M. R. K. is supported by the DFG CRC1436 project 425899996 (A02, also to A. K., A04, Z01, RTG 2413 SynAGE project 362321501, Alzheimer Forschungsinitiative (AFI AFI Grant #23055R) and FOR5228 (RP06 to A. K. and M. R. K.) and the Human Frontier Science Program (RGP0002/2022).

Author contributions—A. W., T. L., A. K., M. R. K., and R. A. writing–review & editing; A. W., T. L., and A. K. writing–original

draft; A. W. and A. K. visualization; A. W. validation; A. W. formal analysis; A. W. and A. K. data curation; T. L., C. N., A. C., and E. C. investigation; A. D., M. R. K., and R. A. resources; M. R. K. and R. A. supervision; M. R. K. and R. A. funding acquisition; M. R. K. and R. A. conceptualization.

Conflict of interest—The authors declare no competing conflict of interest.

Abbreviations—The abbreviations used are: ACN, acetonitrile; AD, alzheimer disease; AGC, automatic gain control; DDA, data dependent acquisition; DEP, differentially expressed protein; DIA, data independent acquisition; DIV, days *in vitro*; FA, formic acid; HFD, high-fat diet; INSR, insulin receptor; iRT, indexed retention time; IRS1, insulin-receptor substrate; IT, injection time; JNK, Jun N-terminal kinase; LC, liquid chromatography; MetS, metabolic syndrome; pAKT, phosphorylated AKT; PPI, protein–protein interaction; PKC, protein kinase C; RD, regular diet; sIR, synaptic insulin resistance; TEAB, triethylammonium bicarbonate; TFA, trifluoracetic acid; tgHFD, transgenic HFD; tgRD, transgenic RD.

Received October 28, 2025, and in revised form, January 20, 2026
Published, MCPRO Papers in Press, February 23, 2026, https://doi.org/10.1016/j.mcpro.2026.101537

REFERENCES

1. Viola, K. L., and Klein, W. L. (2015) Amyloid β oligomers in Alzheimer's disease pathogenesis, treatment, and diagnosis. *Acta Neuropathologica* **129**, 183–206
2. Qureshi, D., Allen, N. E., Kuźma, E., and Littlejohns, T. J. (2025) Metabolic syndrome and risk of incident all-cause dementia, Alzheimer's disease and vascular dementia: a systematic review and meta-analysis of longitudinal studies. *Alzheimers Res. Ther.* **17**, 198
3. Qiu, S. D., Zhang, D. D., Ma, L. Y., *et al*. (2025) Associations of metabolic syndrome with risks of dementia and cognitive impairment: a systematic review and meta-analysis. *J. Alzheimer's Dis.* **105**, 15–27
4. Confettura, A. D., Cuboni, E., Ammar, M. R., *et al*. (2022) Neddylation-dependent protein degradation is a nexus between synaptic insulin resistance, neuroinflammation and Alzheimer's disease. *Transl. Neurodegen.* **11**, 2
5. Alexandru, A., Jagla, W., Graubner, S., *et al*. (2011) Selective hippocampal neurodegeneration in transgenic mice expressing small amounts of truncated Aβ is induced by Pyroglutamate–Aβ Formation. *J. Neurosci.* **31**, 12790–12801
6. Grochowska, K. M., Gomes, G. M., Raman, R., *et al*. (2023) Jacob-induced transcriptional inactivation of CREB promotes Aβ-induced synapse loss in Alzheimer's disease. *EMBO J.* **42**, e112453
7. Dunkelmann, T., Schemmert, S., Honold, D., *et al*. (2018) Comprehensive characterization of the pyroglutamate Amyloid-β induced motor neurodegenerative phenotype of TBA2.1 mice. *J. Alzheimer's Dis.* **63**, 115–130
8. Grochowska, K. M., Yuanxiang, P., Bär, J., *et al*. (2017) Posttranslational modification impact on the mechanism by which amyloid-β induces synaptic dysfunction. *EMBO Rep.* **18**, 962–981
9. Yarbro, J. M., Han, X., Dasgupta, A., *et al*. (2025) Human and mouse proteomics reveals the shared pathways in Alzheimer's disease and delayed protein turnover in the amyloidome. *Nat. Commun.* **16**, 1533
10. Li, T., Wenger, A., Coman, C., Borutzki, C., Kreutz, M. R., and Ahrends, R. (2025) SIMPLEX enriches hydrophobic and lipidated proteins in membrane proteomics experiments. *Proteomics* **25**, 28–39
11. Borgmeyer, M., Coman, C., Has, C., *et al*. (2021) Multiomics of synaptic junctions reveals altered lipid metabolism and signaling following environmental enrichment. *Cell Rep.* **37**, 109797
12. Coman, C., Solari, F. A., Hentschel, A., Sickmann, A., Zahedi, R. P., and Ahrends, R. (2016) Simultaneous metabolite, protein, lipid extraction (SIMPLEX): a combinatorial multimolecular omics approach for systems biology. *Mol. Cell Proteomics* **15**, 1453–1466
13. Manza, L. L., Stamer, S. L., Ham, A. J., Codreanu, S. G., and Liebler, D. C. (2005) Sample preparation and digestion for proteomic analyses using spin filters. *Proteomics* **5**, 1742–1745
14. Dickhut, C., Radau, S., and Zahedi, R. P. (2014) Fast, efficient, and quality-controlled phosphopeptide enrichment from minute sample amounts using titanium dioxide. *Methods Mol. Biol. (Clifton, NJ)* **1156**, 417–430
15. Burkhart, J. M., Schumbrutzki, C., Wortelkamp, S., Sickmann, A., and Zahedi, R. P. (2012) Systematic and quantitative comparison of digest efficiency and specificity reveals the impact of trypsin quality on MS-based proteomics. *J. Proteomics* **75**, 1454–1462
16. Solari, F. A., Kollipara, L., Sickmann, A., and Zahedi, R. P. (2016) Two birds with one stone: parallel quantification of proteome and phosphoproteome using iTRAQ. *Methods Mol. Biol. (Clifton, NJ)* **1394**, 25–41
17. Li, T., Wenger, A., Coman, C., Borutzki, C., Kreutz, M. R., and Ahrends, R. (2025) SIMPLEX enriches hydrophobic and lipidated proteins in membrane proteomics experiments. *Proteomics* **25**, e70016
18. Karpova, A., Samer, S., Turacak, R., Yuanxiang, P., and Kreutz, M. R. (2023) Integration of nuclear Ca2+ transients and subnuclear protein shuttling provides a novel mechanism for the regulation of CREB-dependent gene expression. *Cell Mol. Life Sci.* **80**, 228
19. Schindelin, J., Arganda-Carreras, I., Frise, E., *et al*. (2012) Fiji: an open-source platform for biological-image analysis. *Nat. Methods* **9**, 676–682
20. Snel, B., Lehmann, G., Bork, P., and Huynen, M. A. (2000) STRING: a web-server to retrieve and display the repeatedly occurring neighbourhood of a gene. *Nucleic Acids Res.* **28**, 3442–3444
21. Shannon, P., Markiel, A., Ozier, O., *et al*. (2003) Cytoscape: a software environment for integrated models of biomolecular interaction networks. *Genome Res.* **13**, 2498–2504
22. Bindea, G., Mlecnik, B., Hackl, H., *et al*. (2009) ClueGO: a Cytoscape plug-in to decipher functionally grouped gene ontology and pathway annotation networks. *Bioinformatics (Oxford, England)* **25**, 1091–1093
23. Molania, R., Foroutan, M., Gagnon-Bartsch, J. A., *et al*. (2023) Removing unwanted variation from large-scale RNA sequencing data with PRPS. *Nat. Biotechnol.* **41**, 82–95
24. Kim, H. J., Kim, T., Hoffman, N. J., *et al*. (2021) PhosR enables processing and functional analysis of phosphoproteomic data. *Cell Rep.* **34**, 108771
25. Johnson, J. L., Yaron, T. M., Huntsman, E. M., *et al*. (2023) An atlas of substrate specificities for the human serine/threonine kinome. *Nature* **613**, 759–766
26. Yaron-Barir, T. M., Joughin, B. A., Huntsman, E. M., *et al*. (2024) The intrinsic substrate specificity of the human tyrosine kinome. *Nature* **629**, 1174–1181
27. Loegering, D. J., and Lennartz, M. R. (2011) Protein kinase C and toll-like receptor signaling. *Enzyme Res.* **2011**, 537821
28. Peng, Y., Sigua, C. A., Rideout, D., and Murr, M. M. (2008) Deletion of toll-like receptor-4 downregulates protein kinase C-ζ and attenuates liver injury in experimental pancreatitis. *Surgery* **143**, 679–685
29. Gupta, P., Taiyab, A., and Hassan, M. (2021) Emerging role of protein kinases in diabetes mellitus: from mechanism to therapy. *Adv. Protein Chem. Struct. Biol.* **124**, 47–85
30. Hirosumi, J., Tuncman, G., Chang, L., *et al*. (2002) A central role for JNK in obesity and insulin resistance. *Nature* **420**, 333–336
31. Nawaratne, R., Gray, A., Jorgensen, C. H., Downes, C. P., Siddle, K., and Sethi, J. K. (2006) Regulation of insulin receptor substrate 1 pleckstrin homology domain by protein kinase C: role of serine 24 phosphorylation. *Mol. Endocrinol.* **20**, 1838–1852
32. Bomfim, T. R., Forny-Germano, L., Sathler, L. B., *et al*. (2012) An anti-diabetes agent protects the mouse brain from defective insulin signaling caused by Alzheimer's disease- associated Aβ oligomers. *J. Clin. Invest.* **122**, 1339–1353
33. Hornbeck, P. V., Kornhauser, J. M., Tkachev, S., *et al*. (2012) PhosphoSitePlus: a comprehensive resource for investigating the structure and function of experimentally determined post-translational modifications in man and mouse. *Nucleic Acids Res.* **40**, D261–D270
34. Langlais, P., Yi, Z., Finlayson, J., *et al*. (2011) Global IRS-1 phosphorylation analysis in insulin resistance. *Diabetologia* **54**, 2878–2889

35. Chen, L., Li, Z., Ahmad, N., and Liu, X. (2015) Plk1 phosphorylation of IRS2 prevents premature mitotic exit *via* AKT inactivation. *Biochemistry* **54**, 2473–2480
36. Neukamm, S. S., Toth, R., Morrice, N., *et al*. (2012) Identification of the amino acids 300-600 of IRS-2 as 14-3-3 binding region with the importance of IGF-1/insulin-regulated phosphorylation of Ser-573. *PLoS One* **7**, e43296
37. Partovian, C., Zhuang, Z., Moodie, K., *et al*. (2005) PKCα activates eNOS and increases arterial blood flow *in vivo*. *Circ. Res.* **97**, 482–487
38. Petersen, M. C., Madiraju, A. K., Gassaway, B. M., *et al*. (2016) Insulin receptor Thr1160 phosphorylation mediates lipid-induced hepatic insulin resistance. *J. Clin. Invest.* **126**, 4361–4371
39. De Felice, F. G. (2013) Alzheimer's disease and insulin resistance: translating basic science into clinical applications. *J. Clin. Invest.* **123**, 531–539
40. Hartz, A. M., Bauer, B., Soldner, E. L., *et al*. (2012) Amyloid-beta contributes to blood-brain barrier leakage in transgenic human amyloid precursor protein mice and in humans with cerebral amyloid angiopathy. *Stroke* **43**, 514–523
41. Kawade, N., and Yamanaka, K. (2024) Novel insights into brain lipid metabolism in Alzheimer's disease: oligodendrocytes and white matter abnormalities. *FEBS Open Bio* **14**, 194–216
42. Yin, F. (2023) Lipid metabolism and Alzheimer's disease: clinical evidence, mechanistic link and therapeutic promise. *FEBS J.* **290**, 1420–1453
43. Shen, L., Yang, A., Chen, X., *et al*. (2022) Proteomic profiling of Cerebrum mitochondria, myelin sheath, and synaptosome revealed mitochondrial damage and synaptic impairments in association with 3 × Tg-AD mice model. *Cell Mol. Neurobiol.* **42**, 1745–1763
44. Liu, P., Wang, Z.-H., Kang, S. S., *et al*. (2022) High-fat diet-induced diabetes couples to Alzheimer's disease through inflammation-activated C/EBPβ/AEP pathway. *Mol. Psychiatry* **27**, 3396–3409
45. Liu, Q., Trotter, J., Zhang, J., *et al*. (2010) Neuronal LRP1 knockout in adult mice leads to impaired brain lipid metabolism and progressive, age-dependent synapse loss and neurodegeneration. *J. Neurosci.* **30**, 17068
46. Colgan, L. A., Hu, M., Misler, J. A., *et al*. (2018) PKCalpha integrates spatiotemporally distinct Ca(2+) and autocrine BDNF signaling to facilitate synaptic plasticity. *Nat. Neurosci.* **21**, 1027–1037
47. Wierda, K. D., Toonen, R. F., de Wit, H., Brussaard, A. B., and Verhage, M. (2007) Interdependence of PKC-dependent and PKC-independent pathways for presynaptic plasticity. *Neuron* **54**, 275–290
48. Sánchez-Sarasúa, S., Meseguer-Beltrán, M., García-Díaz, C., Beltrán-Bretones, M. T., ElMlili, N., and Sánchez-Pérez, A. M. (2022) IRS1 expression in hippocampus is age-dependent and is required for mature spine maintenance and neuritogenesis. *Mol. Cell Neurosci.* **118**, 103693
49. Talbot, K., and Wang, H.-Y. (2014) The nature, significance, and glucagon-like peptide-1 analog treatment of brain insulin resistance in Alzheimer's disease. *Alzheimer's Demen.* **10**, S12–S25
50. Hançer, N. J., Qiu, W., Cherella, C., Li, Y., Copps, K. D., and White, M. F. (2014) Insulin and metabolic stress stimulate multisite serine/threonine phosphorylation of insulin receptor substrate 1 and inhibit tyrosine phosphorylation. *J. Biol. Chem.* **289**, 12467–12484